Modelling reconstruction and boulder size-frequency distribution of a young (

Maurizio Pajola, Martin Mergili, Pamela Cambianica, Alice Lucchetti, Maria Teresa Brunetti, Anthony Guimpier, Maria Mastropietro, Giovanni Munaretto, Susan J. Conway, Joel Beccarelli, et al.

Modelling reconstruction and boulder size-frequency distribution of a young (< 5 Myr) landslide located in Simud Vallis floor, Mars.

Pajola Maurizio[1], Mergili Martin[2], Cambianica Pamela[1], Lucchetti Alice[1], Brunetti Maria Teresa[3], Guimpier Anthony[4], Mastropietro Maria[5], Munaretto Giovanni[6,1], Conway Susan[4], Beccarelli Joel[6], Cremonese Gabriele[1].

[1] INAF, Astronomical Observatory of Padova, Vic. Osservatorio 5, 35122 Padova, Italy (maurizio.pajola@inaf.it)
[2] University of Graz, Graz, Austria
[3] Research Institute for Geo-Hydrological Protection-Italian National Research Council, Perugia, Italy,
[4] Laboratoire de Planétologie et Géodynamique, UMR6112 CNRS, Université de Nantes, France
[5] Braunschweig TU University, Braunschweig, Germany
[6] University of Padova, Padova, Italy

Abstract

We focus on a young (~ **4.5 Ma**), 3.4 km long landslide located in the floor of Simud Vallis, Oxia Palus Quadrangle of Mars. By making use of a **2 m-scale** HiRISE DEM we reconstruct the terrain surface before the landslide and in doing so we estimate the release and deposition heights and volumes related to the different stages of the landslide. Using the *r.avaflow* software we simulate the mass movement as a multi-stage event, and obtain simulated deposits that are both spatially and longitudinally comparable to the current landslide deposits. Through two 0.25 m-scale HiRISE images we identify and manually count > 130 000 boulders that are located along the landslide, deriving their size-frequency distribution and spatial density per unit area for boulders with an equivalent diameter ≥1.75 m. Our analyses reveal that the distribution is of a Weibull-type, suggesting that the rocky constituents fractured and fragmented progressively during the course of the mass movement, consistent with our proposed two-stage model of landslide motion.

1.0 Introduction

During the last 50 years multiple planetary exploration missions have collected high-resolution images of Solar System bodies, which have been sufficient to detect and identify detailed structures and scales of surface landforms, such as landslides. Using as a reference similar structures observed on Earth (terrestrial analogues) and using the same classification system, we observe that the characteristics of landslides on other solid bodies can be just as variable as those on Earth (**Hargitai and Kereszturi, 2015**).

So far, landslides have been observed on Mercury (Xiao and Komatsu, 2013; Blewett et al., 2013; Brunetti et al., 2015), Venus (Malin, 1992), the Moon (Pike, 1971; Lindsay, 1976; Xiao et al., 2013; Brunetti et al., 2015), Phobos (Shi et al., 2016), asteroids (Massironi, et al., 2012; Magrin et al., 2012; Duarte et al., 2019; Jawin et al., 2020), icy satellites (Schenk and Bulmer, 1998; Chuang and Greeley, 2000; Singer et al., 2012, Beddingfield et al., 2021) and comets (Lucchetti et al., 2019). Among terrestrial planets, Mars has been the most studied with respect to landslides (e.g., Lucchitta, 1979; McEwen, 1989; Shaller and Komatsu, 1994; Quantin et al., 2004; Soukhovitskaya and Manga, 2006; Bigot-Cormier and Montgomery, 2007; Lucas and Mangeney, 2007, Brunetti et al., 2014; Crosta et al., 2018). **On Mars, landslides generally much larger than the terrestrial subaerial ones**[1] are located on slopes (Sharp, 1973) in

[1] **Landslides in Valles Marineris, which are among the largest found on Mars, are comparable in size to the largest submarine landslides of the Earth (Brunetti et al., 2014).**

canyons (e.g., Valles Marineris), as well as on mountainous reliefs (e.g., Olympus Mons) and crater structures.

As on Earth, the morphology (e.g., area, volume, runout length, drop height, width, and texture) of the landslide deposit on extra-terrestrial bodies depends on factors such as the slope of the topography, the collapse mechanism, the mechanical properties of the material, the presence of fluids and volatiles within the sliding material, and the local environmental conditions (e.g., the gravitational acceleration). Potential landslide preparatory and triggering factors, on the other hand, can vary from one planet to another. For example, on Earth the presence of a thick atmosphere means the main cause of landslides is rainfall, whereas on Mars the low-density atmosphere means this mechanism cannot be inferred for recent landslides. Because we have never directly observed any Martian landslide, their preparatory and triggering factors have to be inferred from their morphology and context. Terrestrial analogues, although useful to infer these factors, are limited because they are not the same size and are directly or indirectly influenced by liquid water. On Mars, the landslides in Valles Marineris have been suggested to be caused by meteorite impacts: either directly caused by the impact-shaking or as a consequence of the decrease in the rock cohesion and potentially the subsequent increase of ground water flowing through the pore fraction (Crosta et al., 2014). According to Kumar et al. (2019), recent (last thousands of years) seismic shaking would be the cause of rock falls along the Martian slopes. The same type of landslide observed on impact crater slopes was also attributed to thermal-stress (Tesson et al., 2020). Recently, Bishop et al. (2021) suggested that the occurrence of Martian landslides could be related to the subsurface cryosalt expansion. They used analogue field investigations on Earth and laboratory experiments to demonstrate that when salts interact with gypsum or water underground, it can cause disruptions on the surface, and may trigger collapses and landslides. The wide range of hypotheses for potential causes of Martian landslides shows that, the lack of direct Earth analogues makes the precise identification of the preparatory and triggering factors of landslides on Mars challenging, with the potential role of water and/or active tectonics being actively debated within the scientific community.

Recently, Guimpier et al. (2021) focussed on three small and **young (with estimated ages not exceeding 20 Ma)** Martian landslides with volumes $< 10^{10}$ m^3, with the main aim to compare them with similarly sized terrestrial analogues. In particular, by using the Mars Reconnaissance Orbiter's (MRO, Zurek et al., 2007) High Resolution Imaging Science Experiment images (HiRISE, McEwen et al., 2007), Guimpier et al. (2021) identified and studied a landslide that is located in Simud Vallis (Oxia Palus quadrangle), a large outflow channel that together with Tiu Vallis once connected the Valles Marineris with the Chryse Planitia (Pajola et al., 2016a, Fig. 1A, B). On Simud Vallis' floor multiple teardrop-shaped islands are present, all elongated in the S-N direction of the flow (Carr and Clow, 1981) that incised the Mid-Noachian plateau (Tanaka et al., 2014; Pajola et al., 2016a). On the western side of one of such landforms (Fig. 1C), is the Simud Vallis landslide (hereafter called *SV landslide*), Fig. 1D, characterised by numerous boulders on its deposits. **In particular, by estimating the maximum age of formation of this landslide through the use of the crater-size frequency distribution (Michael and Neukum, 2010) technique (we underline that only one 23 m size crater is identified on the SV deposits), Guimpier et al. (2021) derived a modelled age of ~ 4.5 $\pm$ 4 Ma: hence the SV landslide formed recently, i.e. during the Late Amazonian period of Mars geochronology.**

By using Earth-Mars comparative morphological analyses performed through similar resolution Digital Elevation Models (DEMs), Guimpier et al. (2021) inferred that the triggering processes of this landslide could have been the shaking by a meteorite impact or a marsquake and the dynamics of the landslide was similar to a dry rock avalanche. As highlighted in Guimpier et al. (2021), the *SHALTOP* numerical modelling (Bouchut et al., 2003; Bouchut and Westdickenberg, 2004; Lucas and Mangeney, 2007) applied on the SV landslide was not conclusive, and further numerical tests are needed to achieve a better representation of the mass movement and its final shape in order to better understand the landslide dynamics (e.g. wet vs dry flow). Guimpier et al., (2021) did not study the size-frequency distribution (SFD) of boulders that characterise the landslide's surface. Yet, as shown by previous studies on the Moon (Cintala and McBride, 1995; Bart and Melosh, 2010; Khrishna and Kumar, 2016; Pajola et al., 2019), asteroids (Geissler et al., 1996; Thomas et al., 2001; Küppers et al., 2012; Mazrouei et al., 2014; Burke et al., 2021, Schröder et al., 2021a), comets (Pajola et al., 2015; Mottola et al., 2015; Pajola et al., 2016b,c; Pajola et al., 2017a,b), icy satellites (Pajola et al., 2021) and Mars (Garvin et al., 1981; Grant et al., 2006; Golombek et al., 2008; Pajola et al., 2017c; Mastropietro et al., 2020) the form of the SFD of blocks/boulders can provide important information on how the parent rock was broken up and on the associated formative and degradation processes.

In this work, we therefore aim to understand in detail how the initial mass moved and fragmented using numerical **modelling** and by quantifying the boulder SFD, hence providing insights into "recent" surface process that may still be occurring elsewhere on Mars.

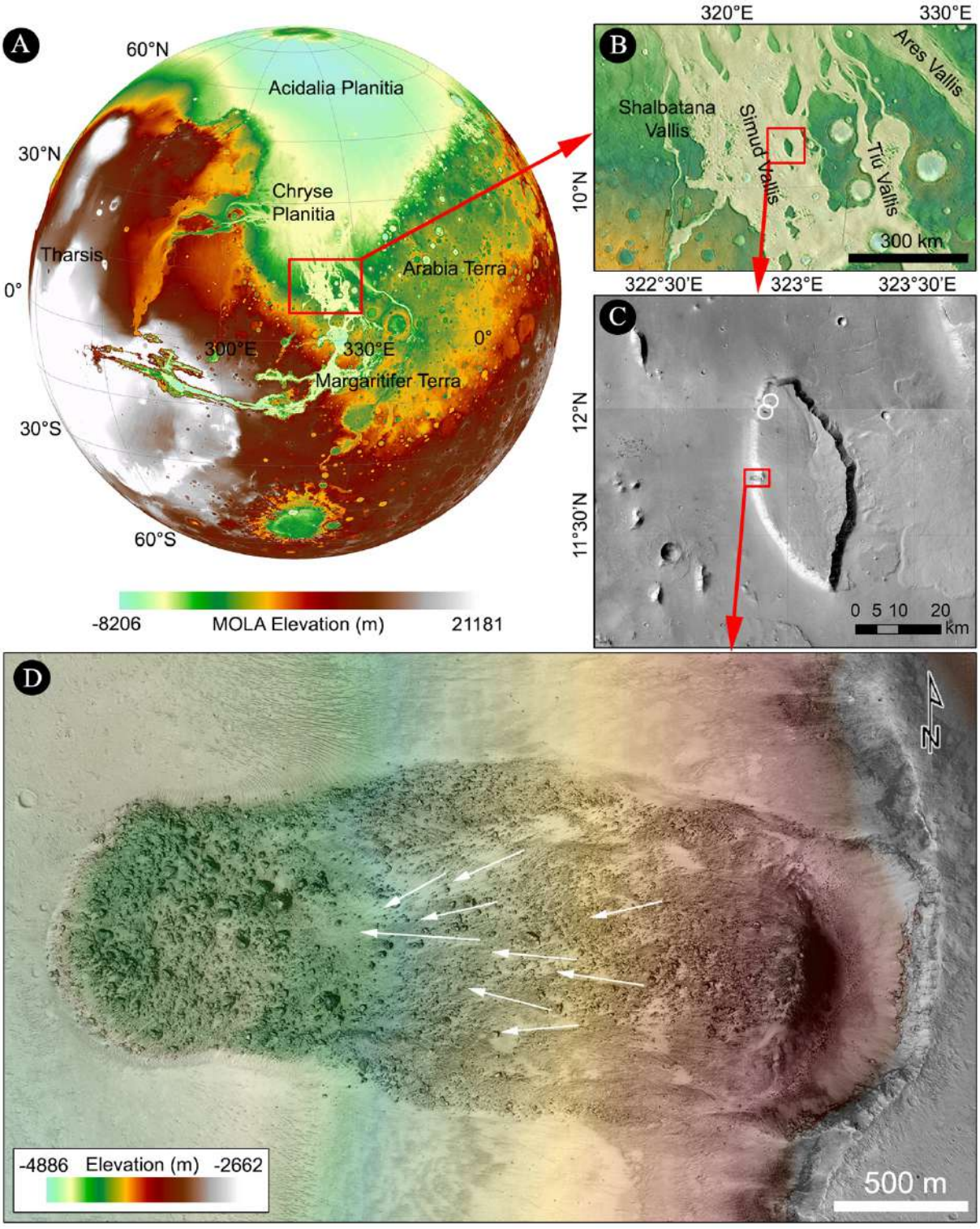

Figure 1: A-B) The location of the Simud Vallis study area on Mars. C) The teardrop-shaped island where the SV landslide is located. **The white circles show other locations where circular-shaped erosion zones are identified, as well as degraded deposits at their feet.** D) The HiRISE ESP_050033_1920 image (see Dataset and Methodology, Table 1) showing the SV landslide, together with the elevation values (in metres) derived from the HiRISE DTM overlaid in transparency. **The white arrows indicate the set of trenches that align parallel to the local direction of motion.**

2.0 Datasets and Methodology

2.1 Imagery and DEM

The SV landslide was first observed with the HiRISE camera in October 2007 with a phase angle of 36.2°, an incidence angle of 41.0° and an original image scale of 0.28 m/pixel. In March 2017 the landslide was again imaged through HiRISE, with a phase angle of 60.9°, an incidence angle of 34.0° and a spatial scale of 0.32 m/pixel. The details for each acquisition are presented in Table 1, the original imagery dataset can be downloaded from www.uahirise.org/PSP_005701_1920 and www.uahirise.org/ESP_050033_1920, while the resulting anaglyph is presented in Supplementary Material Fig SM1. **The slightly different observing conditions (both illumination and geometry of the acquisitions)** of the two images provided the possibility to prepare a DEM of the landslide through the Ames Stereo Pipeline (Moratto et al., 2010) with a spatial resolution of 2 m (Guimpier et al., 2021), Fig. 1D. This product has been vertically controlled to ESA's Mars Express High Resolution Stereo Camera (HRSC, Neukum and Jaumann, 2004) publicly available DEMs.

HiRISE Image ID	Acquisition Date	Pixel Scale (m)	Local Time (hh:mm)	Phase Angle (°)	Incidence Angle (°)	Emission Angle (°)
PSP_005701_1920	14/10/2007	0.25	14:12	36.2	41.0	5.0
ESP_050033_1920	30/03/2017	0.25	13:51	60.9	34.0	28.7

Table 1: HiRISE image ID, date of acquisition, map projected (equirectangular) pixel scale, local time and observing angles of the images used for the DEM generation.

The mentioned 2 m-scale DEM is extremely useful to both evaluate the post-collapse surface topography and to reconstruct the pre-landslide terrain including its longitudinal profile. These are pivotal aspects to then simulate the landslide formation and subsequent movement. Moreover, the acquired images are characterised by shadows (if they were absent, they would hamper the boulder identification, if they were too elongated, they would cover nearby features) that are optimal for the detailed identification of the boulders located in the landslide deposits, hence providing the possibility to perform a size-frequency distribution (SFD) analysis.

2.2 Terrain and event reconstruction

By making use of the HiRISE 2 m-scale DEM (Fig. 1D) we first distinguish the circular-shaped erosion zone where the Simud Vallis landslide detached, its longitudinal profile down to the deposit zone, the sharp front, as well as the lateral levees. We then identify the most likely sequence of mechanisms involved in the event. Based on the qualitative, manual interpretation of visible terrain features, we suggest a two-stage model of the event. Stage 1 represents a rotational slide, stopping and depositing still in the upper portion of the slope (overlap of scarp and deposit). Stage 2 starts through the immediate or delayed mobilization of part of the deposit, and propagates down the entire slope as a viscous flow-type movement (see Discussion for a more detailed interpretation).

On this basis, we reconstruct the terrain surfaces prior to the landslide and estimate the release and deposition heights and volumes related to the different stages of the SV landslide. The terrain reconstruction (Fig. 2A, B) is realised by manual construction of contour lines and their

subsequent interpolation, representing four situations (Fig. 2A a-e): (a) the terrain before stage 1; (b) the basal surface of stage 1; (c) the terrain after stage 1, but before stage 2; (d) the basal surface of stage 2. The post-event situation (e) is represented by the existing DEM. The release height of stage 1 is derived as (a) – (b), the deposition height of stage 1 as (c) – (b), the release height of stage 2 as (d) – (c), and the deposition height of stage 2 as (e) – (d). Thereby, we build on the assumption that (i) the pre-event topography was characterized by a smooth and straight connection of the terrain elements around the landslide **– this assumption was implemented by connecting the corresponding contour lines on both sides of the landslide by a straight reconstructed contour lines, and interpolating those vector data to a DTM;** (ii) volumes were conserved during the landslide (no material has entered or left the system); (iii) during the flow-like stage 2 of the landslide, disintegration of the landslide mass generated a pore space of 20% of the volume.

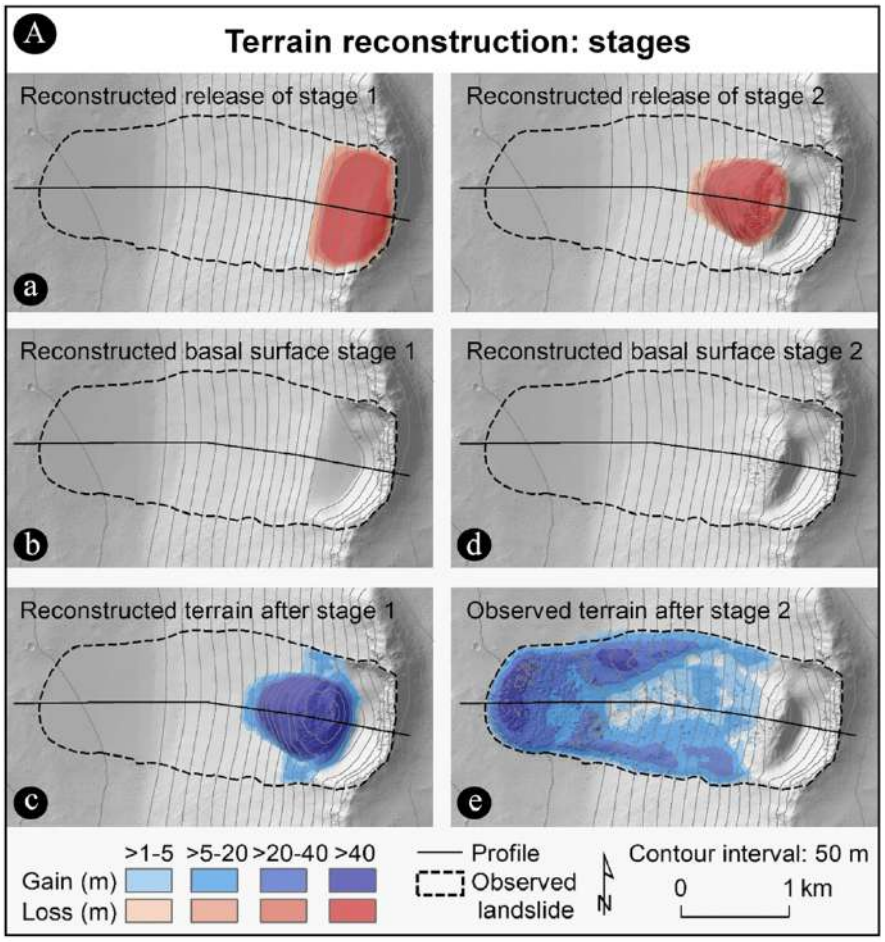

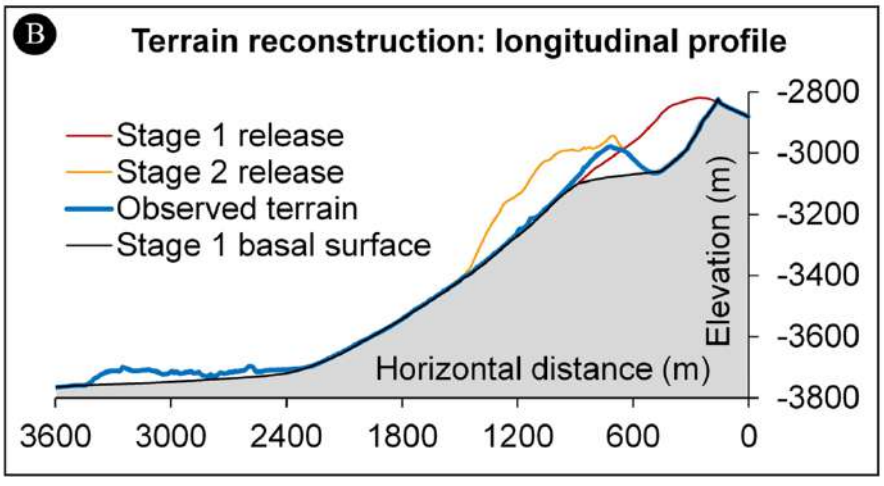

Figure 2: Terrain reconstruction. A) Shaded relief map with release heights (loss) and deposition heights (gain) of both stages. The different stages from (a) to (e) are detailed in the main text. B) Longitudinal **profiles**. Note that horizontal and vertical scales are different.

2.3 Simulation of stage 2

Guimpier et al. (2021) modelled the SV landslide (called Chryse Chaos landslide, ChrC, in that work) with the numerical simulation software *SHALTOP*. Results showed some moderate correspondence between the observed and the simulated flow areas and deposits, and the authors concluded that their results are not fully conclusive regarding the mechanism. *SHALTOP* represents a comparatively simple flow model, where the dynamics of the movement strongly depend on the basal friction angle as the dominant material parameter, but where viscosity cannot be considered. *SHALTOP* has been successfully applied to processes such as lahars (Peruzzetto et al., 2021), but its rheological assumptions might be not fully suitable for the SV landslide with a presumably rather viscous behaviour. Further, Guimpier et al. (2021) assumed a relatively confined release area in the centre of the stage 1 deposit which, in our opinion, is not necessarily fully supported by observations. Therefore, we re-evaluate the dynamics of the SV landslide using the mass flow simulation framework *r.avaflow* (Mergili et al., 2017; Mergili and Pudasaini, 2021), with our reconstructed release area and the assumption of a more viscous flow, taking into account the gravitational acceleration on Mars of 3.72 $m \cdot s^{-2}$. Thereby, the multi-stage flow model of Pudasaini and Mergili (2019) is applied. **For the sake of simplicity, we reduce the flow mass to one stage of a viscosity-dominated viscoplastic material, which is assumed to consist of fragments of basaltic rock with a density of 3000 $kg \cdot m^{-3}$. The Pudasaini and Mergili (2019) model considers the grain density (i.e. the density of the basalt in this case), and not the bulk density including the pore space.** The flow is assumed to stop as soon as its kinetic energy drops below 5% of the maximum kinetic energy reached throughout the motion. Friction and viscosity parameters are optimized through a step-wise iterative procedure, targeting at the best possible reproduction of the travel distance as well as the extent and thickness of the observed landslide deposit. Simulations are run at a raster cell size of 10 m.

2.4 Boulder identification and SFD

We imported the map projected HIRISE images and the **2 m-scale** DEM into the ArcGIS environment, which is commonly used for planetary landform analysis (Pajola et al., 2017c; Mastropietro et al., 2020, Burke et al., 2021). Following the Burrough and McDonnel (1998) methodology we computed the surface slope of the area (Fig. 3A), using it to identify both the extent of the SV landslide as well as those of the largest boulders. We then visually identified the landslide boulders based on their shape and slope boundary (Fig. 3A), defining them as positive reliefs detectable through the presence of a nearby elongated shadow (Fig. 3B). Afterwards, their outline was manually approximated by a polygon (Fig. 3C), extracting their areas and returning the linear metric size as the diameter of a circle with the same area as the polygon.

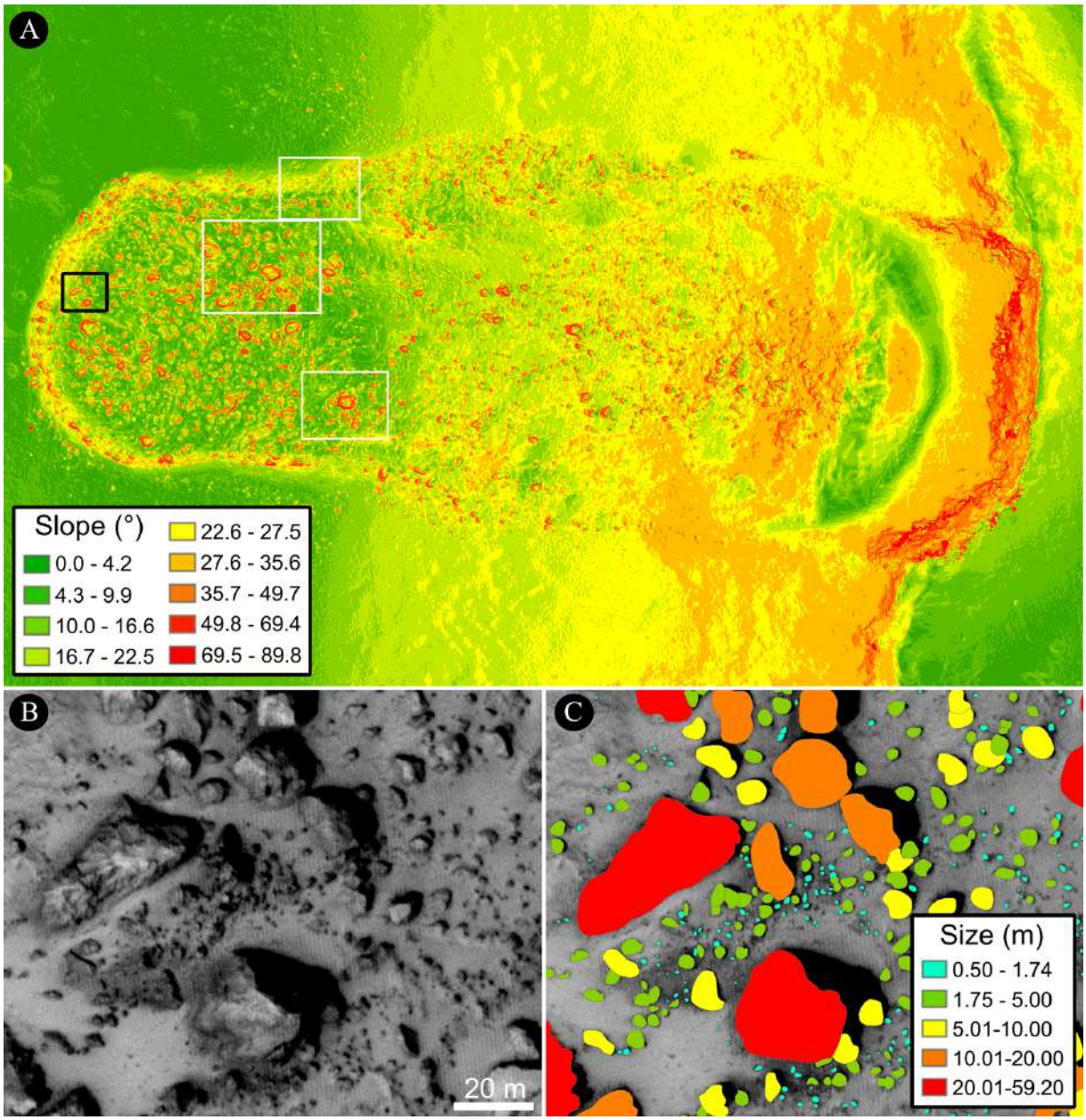

Figure 3: A) Slope map of the SV landslide surface and boulders. The slope values (in degrees) are grouped in coloured bins. The black box outlines the extension of Fig. 3B and C, **while the black boxes outline the extension of Fig. SM2 A-F**. B) HiRISE uninterpreted closeup image showing the presence of multiple boulders. C) Same as B, but with the identified boulders grouped by size.

The solar incidence angle and the height of the boulder **cause** uncertainties in the determination of the boulder shape because of the shadows. For example, at constant height, the smaller is the incidence angle, the smaller is the shadow. Other sources of error include the ability to reliably distinguish boulders from non-boulders features, such as small hills, mounds or portions of bedrock escarpments (Golombek et al., 2008). As previously done for HiRISE images, we decided to consider as statistically meaningful only those boulders with a diameter larger than 1.75 m (Pajola et al., 2017c; Mastropietro et al., 2020), i.e. 7 HiRISE pixels, hence reducing the possibility of feature misinterpretation. **We underline that some of the largest identified boulders are characterised by deep cracks and fractures (see the Discussion section of the manuscript) which could lead to the erroneus count of multiple boulders, instead of single ones. The continuity of the overall boulder shape means that we can determine if nearby**

chunks belong to the same feature, and so we decided to count the fractured boulders as single ones, hence not affecting the resulting diameters (Supplementary Material Fig SM2 A-D). Another point to be considered is the fact that there are some boulders in the landslide deposit that are mantled by dust. The correct size identification is then difficult, because we can only measure the exposed part of the boulder, and we cannot infer what lies underneath (Supplementary Material Fig SM2 E, F). Nevertheless, we believe that given that the smallest sizes we identified (i.e. those boulders that should be most affected by a dust blanket) are not used for the SFD analysis, we assume that the obtained results are not significantly affected by this aspect. After the identification of the boulders, we determined the area over which they are found to 3.03 km^2. This is done in order to obtain the boulder density per unit area. We then derived the boulder SFD, using a log-log plot, where the *x* axis is the boulder size in meters and the *y* axis is the cumulative number of boulders per km^2. Afterwards, the data are fitted with multiple curves (power-law, exponential-law and Weibull) that are commonly used for boulder SFD fitting studies on different planetary and minor bodies surfaces (Golombek and Rapp, 1997; Michikami et al., 2008, Küppers et al., 2012; Pajola et al., 2019; Schröder et al., 2021b), in order to evaluate which one better represents the data.

3.0 Results

The SV landslide forms a 3.4 km long feature that is located at 11°43'N, 322°54'E, in a region that Tanaka et al. (2014) described as "Hto" unit, i.e. an Hesperian transition outflow unit constituted by fluvial deposits of both Tiu and Simud Valles. A more detailed geological analysis done by Pajola et al. (2016a) reported multiple evolutionary stages (occurring from after Middle Noachian to Late Amazonian), with possible flow inversions and ponding. In particular, the SV landslide is situated on the west-flank of a flat-topped teardrop-shaped island (also called a mesa) in the middle of the Simud Vallis' floor, rising up to ~950 m above it (Fig. 1B, D). The island's top has a Middle Noachian modelled age and it is characterised by the presence of friable sediments, impact debris, as well as volcanic material (Tanaka et al., 2014; Pajola et al., 2016a). As detailed in the morphometric section of Guimpier et al. (2021), the erosion zone of the studied landslide has a maximum length of 450 m, a maximum width of 1150 m and its slope ranges between 27° and 85° (Fig. 3A). In addition, the transport zone has a total length of 1700 m, a maximum width of 1300 m and a mean slope of 23°. Finally, the deposit zone has a total length of 1100 m and a maximum width of 950 m. It presents slope values between ~2° to < 10°, while its front scarp slope ranges between 18° and 29°.

The studied landslide and its circular-shaped erosion zone are not the only ones present on the flanks of the teardrop-shaped island. Indeed, two other similar eroded shapes are present in the north-western flanks of the Simud mesa (Fig. 1C, white circles). Nevertheless, the studied SV landslide is the only one with clearly recognisable boulders across the deposit without significant aeolian mantling and the appearance of the boulders is fresh.

3.1 Terrain and event reconstruction

Fig. 2A and B shows the reconstructed release and deposition heights of both stages of the SV landslide. For stage 1, we suggest a rotational slide with a total volume of $54.0 \cdot 10^6$ m^3. We assume a deforming, but not disintegrating moving mass, characterized by identical release and deposition volumes. **Deformation of the sliding mass was certainly necessary to conform to the terrain (a completely rigid block would not have been able to move in the way shown**

by available evidence), and is also indicated by the shape of the remaining intermediate deposit. If there had been immediate disintegration (i.e. the transformation from a slide-dominated movement to a flow-dominated movement), it would have been expected that the mass would have immediately moved down to the base of the slope (as it did in stage 2), and would not have formed the clearly visible intermediate deposit. $13.4 \cdot 10^6$ m³ of the stage 1 deposit remain in place after stage 2 (shown in the post-event DEM). This means that a stage 2 release volume of $40.6 \cdot 10^6$ m³ has to be imposed in order to achieve the stage 1 deposition of $54.0 \cdot 10^6$ m³. The post-event DEM reveals a deposited volume of $48.7 \cdot 10^6$ m³ for stage 2. This means a volume increase of 20% due to the generation of pore space during the flow, corresponding to the target value defined in the methods section. This confirms the overall plausibility of the reconstruction, even though some details (the exact shape of the stage 1 deposition / stage 2 release mass in particular) remain uncertain.

3.2 Simulation of stage 2

The stage 2 flow is numerically reconstructed with the *r.avaflow* software. Empirical optimization of the key model parameters results in an internal friction angle of 40°, a basal friction angle of 15°, a kinematic viscosity of 162 m^2s^{-1}, and a yield strength of 40 Pa. Fig. 4A illustrates the simulated evolution of the flow height. The general patterns of the flow, including the formation of a sharp front and lateral levees, is plausibly reproduced by the simulation. The height of the deposit is slightly overestimated in the frontal part, particularly when considering that the model result does not include the assumed 20% pore space of the observed deposit (Fig. 4B). The most notable deviation between simulation results and observation consists in the minor southward turn of the mass in the relatively flat deposition area, where the terrain very slightly drops southward by approximately 0.8°. The observed deposit does not show any sign of turning southward. This phenomenon is considered in more detail in the Discussion section.

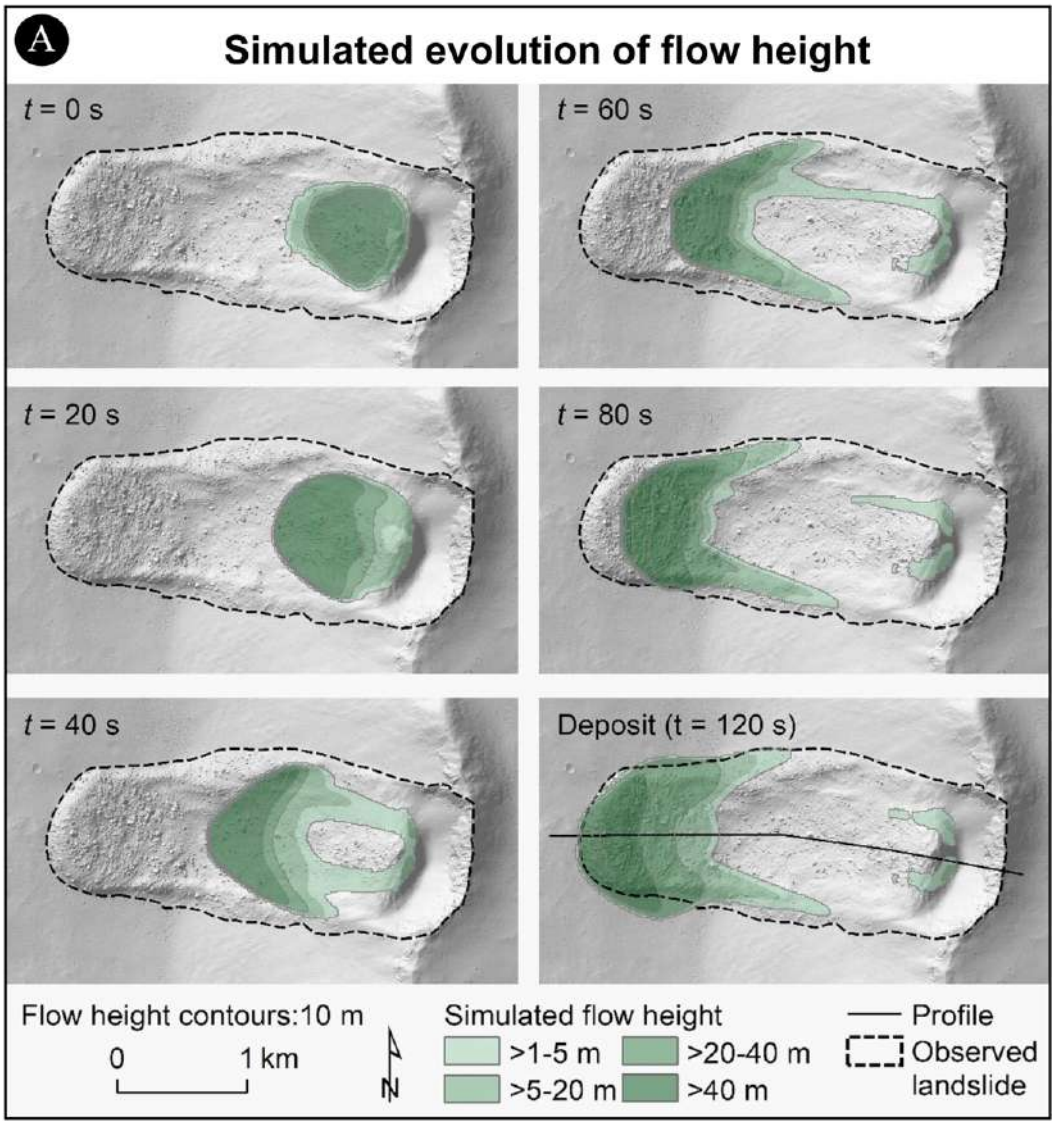

299

300 Figure 4: Simulated evolution of the flow height of the second stage of the SV Landslide. A) Shaded
301 relief map with flow heights at different points in time. B) Longitudinal profile showing the comparison
302 of the observed and the simulated stage 2 deposits. Note that horizontal and vertical scales are different.
303 Simulated flow heights and deposit exclude pore space in both A and B.

304

3.3 Boulder SFD

We manually identified 130 597 boulders at the surface of the SV landslide (Fig. 5), with a minimum size ~ 0.5 m and a maximum size reaching 59.2 m. As explained in the Methodology section all boulders < 1.75 m are excluded from the statistics, in order to avoid possible feature misinterpretation (Fig. 6A). The total number of identified boulders ≥ 1.75 m is 24 073, **with an areal density** of 7945 km^{-2} for a size of 1.75 m (Fig. 6B). The density value decreases to 4595 km^{-2} at a size of 2.5 m, 1674 km^{-2} at 5 m and 391 km^{-2} for 10 m size boulders.

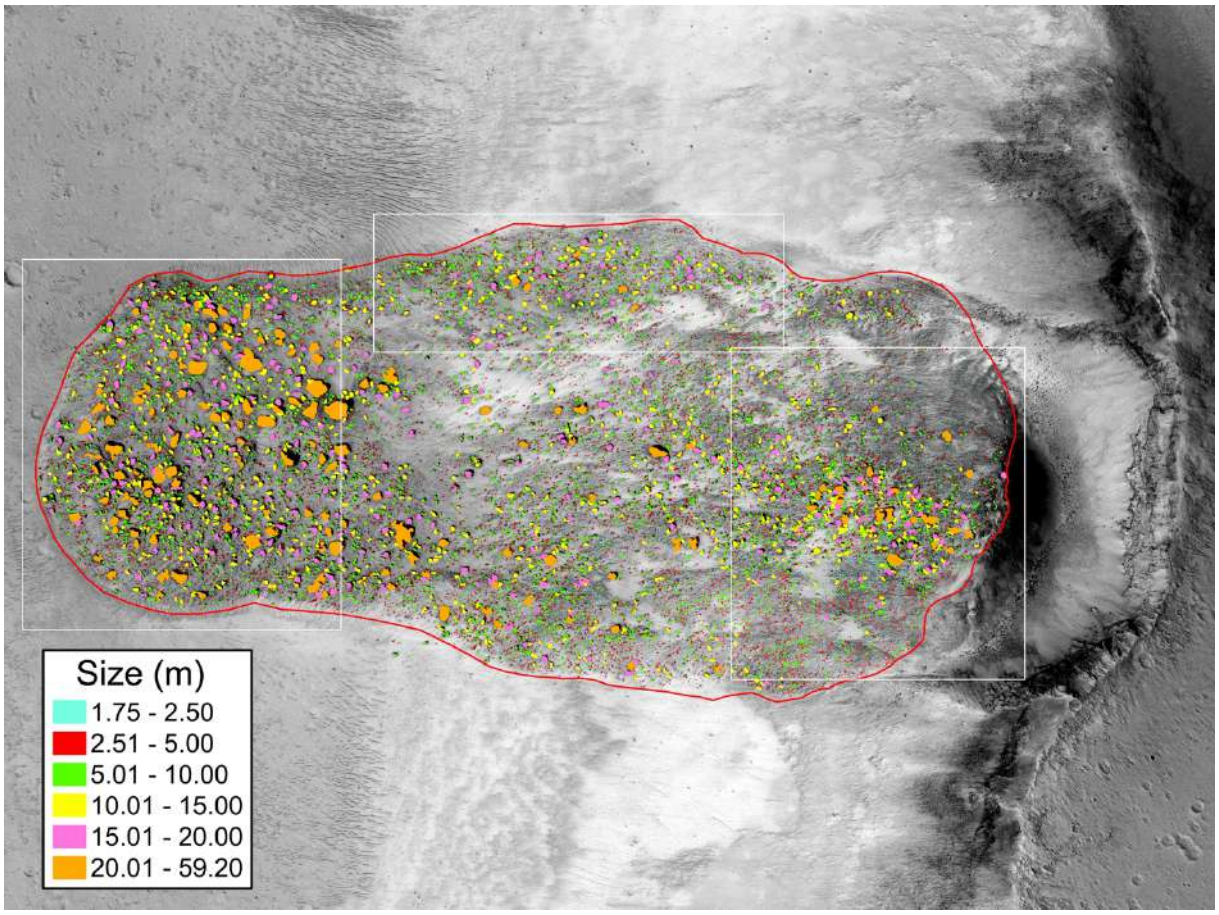

Figure 5: The spatial distribution of all boulders ≥ 1.75 m identified in the SV landslide. The boulder sizes (in metres) are grouped in coloured bins. The red polyline identifies the area (3.03 km^2) where we counted the boulders, while the white boxes outline the close-up views that are presented in Supplementary Material Fig. SM3.

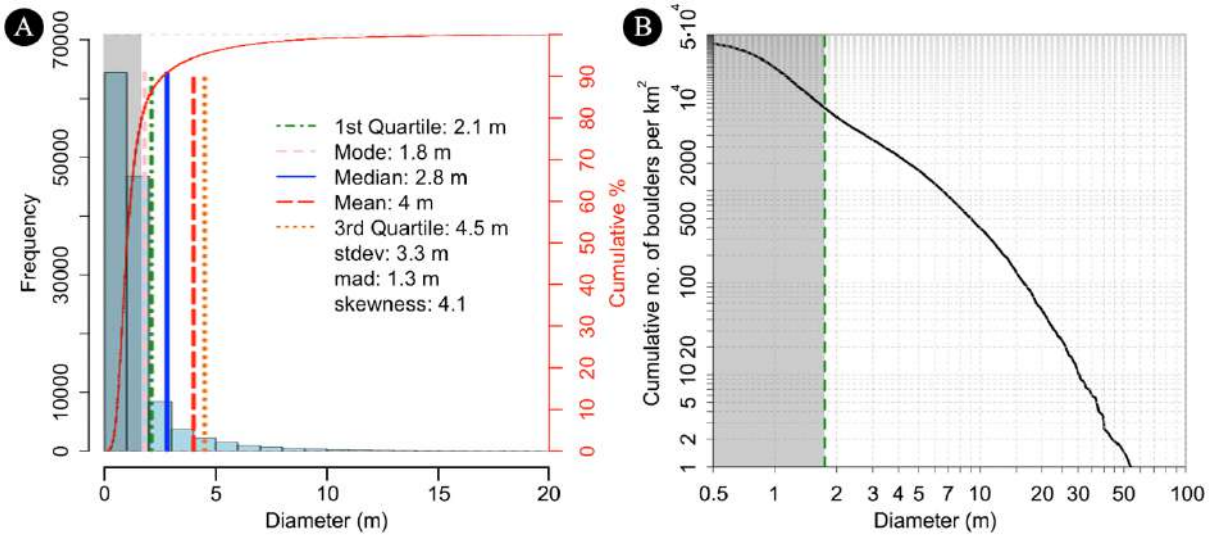

317

318 Figure 6: A) Frequency histogram of all boulders identified in the red area outlined in Fig. 5. The grey
319 shadowed area shows the boulders that have been identified, but their size is < 1.75 m. The main
320 statistical properties of the right-skewed distribution are computed **only for size values** ≥ 1.75 m. B)
321 Log-log plot showing the cumulative number of boulders per km^2. As for A, the grey shadowed area
322 indicates all boulders < 1.75 m.

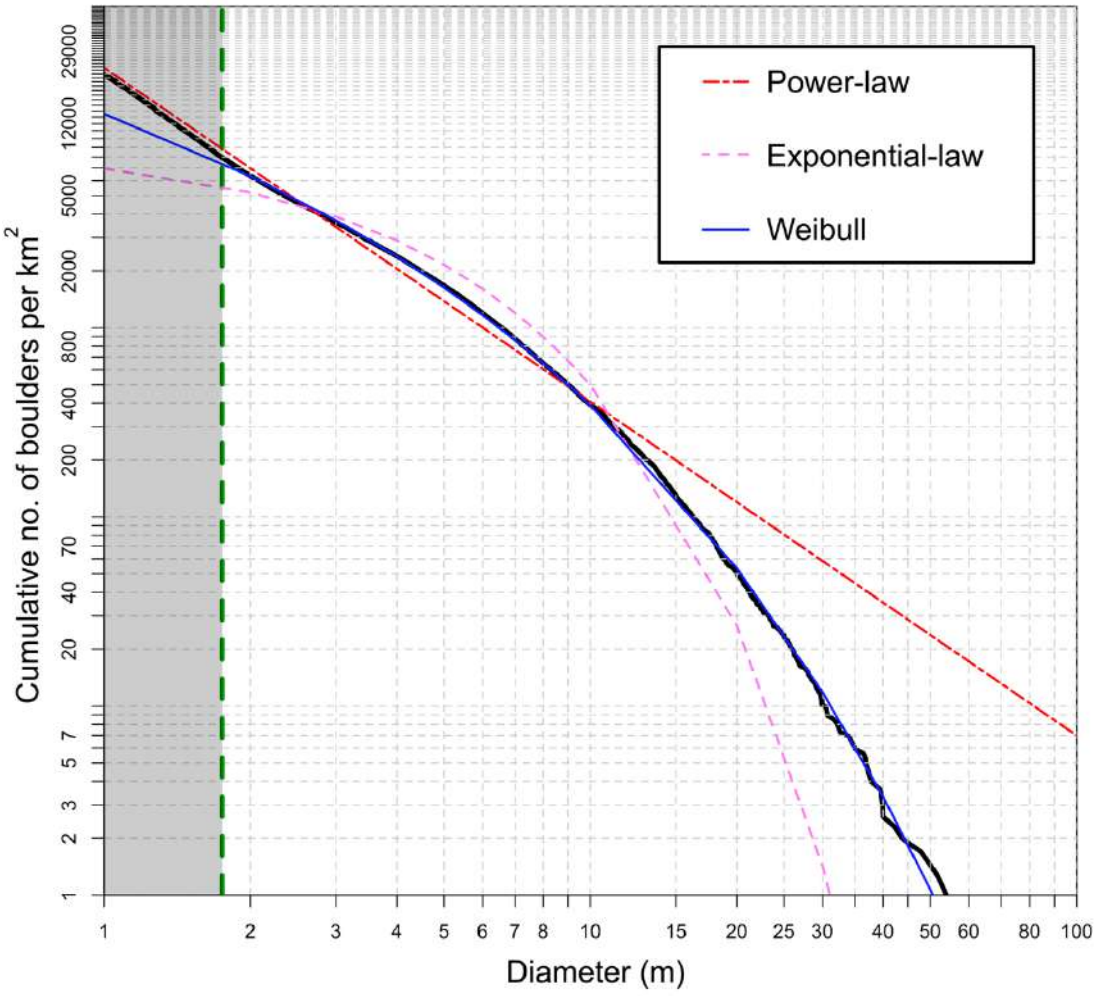

323

324 Figure 7: Cumulative number of boulders per km^2 with the three different fitting curves computed in the
325 1.75 m – 59.2 m size range. As for Fig. 6, the grey shadowed area shows boulders < 1.75 m, not
326 considered by the multiple fits.

We then fitted three different curves on the cumulative number of boulders per km^2: a power-law, an exponential-law and a Weibull distribution, for the size range 1.75 m – 59.2 m. For each case we used the corresponding R^2 value to evaluate the quality of the fit.

In particular, since in our computation we solely include boulders larger than a certain size in the fit, we could use the Weibull left-truncated distribution with the cumulative form of Wingo (1989):

$$N\,(>d) = N\exp[-\alpha(d_i^{\beta} + d_{min}^{\beta})],$$

where N is the number of boulders larger than d_{min}, while α and β are the Weibull parameters estimated from the boulder sizes $d_i > d_{min}$. The resulting best fits are presented in Fig. 7. The power-law fitting curve is characterised by an index of -1.77 and an R^2 value of 0.97, while the exponential-law curve has an exponent of -0.29 and a R^2 of 0.93. On the contrary, the Weibull best fitting curve which returns a R^2 value of 0.99 is characterised by an α value of 1.09 and a β value of 0.57.

4.0 Discussion

The identification and mapping of landslides on Mars uses the same visual criteria adopted for terrestrial landslides when interpreting aerial photographs or satellite images. These criteria include shape, size, tone, texture, object pattern, site topography, and setting[2] (Guzzetti et al., 2012). Mass movements are classified based on their morphological similarity with terrestrial landslide types (Cruden and Varnes, 1996; Hungr et al., 2014). The main types of mass movements recognized on Mars are: (i) slides (RS), including rock slides and deep-seated slides, (ii) complex/compound slides (CL), (iii) rock avalanches (RA), (iv) debris flows (DF), including debris avalanches and shallow debris slides, and (v) rock glacier-like features (RG) (Brunetti et al., 2014).

Based on the visual criteria, the SV landslide can be interpreted as a complex landslide (CL) involving both a rotational slide and a flowing component. Moreover, the landslide deposit exhibits a set of trenches (**white arrows in Fig. 1D**) that align parallel to the local direction of motion. This could be indicative of a likely rapid-to fast-moving flow mechanism for the emplacement of failed materials (Pierson and Costa, 1987).

The post-event terrain, the derived reconstruction of the pre-event terrain, as well as the release mass support the hypothesis of a rotational slide (slump) during stage 1. There is little evidence to conclude or even to speculate on the velocity of the stage 1 event, which might have been anything from extremely slow to extremely rapid, according to the classification of Cruden and Varnes (1996). However, it appears very likely that a major fraction of the stage 1 landslide deposited on the steep slope beneath the circular-shaped landslide scar (Fig. 2A-B). This opens the question on the mechanisms and timing of the transition from stage 1 to stage 2.

[2] The pattern of an object is its spatial arrangement in a repeated or typical order or form. The site topography is the position with reference to its surroundings. The setting refers to regional and local characteristics (lithological, geological, morphological, climatic, etc.) in relation to the surroundings. Site topography and setting are used to infer rock type and structure, attitude of bedding planes, and the presence of faults and other tectonic or structural features (Guzzetti et al., 2012).

In principle, the evidence supports two idealised scenarios, or a combination of both:

I. The material mobilised in the stage 1 rotational landslide entered the steep downslope area. It was continuously remobilised through the stage 2 flow process, continuing as long as material was supplied from upslope, starting either immediately or after a threshold of load was reached;
II. The stage 1 landslide material deposited on the steep slope remained in place until a threshold was reached, and then moved at once, forming the stage 2 flow.

The steep-fronted, largely unstructured deposition lobe of the stage 2 flow supports scenario II. However, there seem to be at least two generations of levees: smaller linear features are located within the area bounded by large levees (see Fig. 3A and Fig. 5). This might indicate a multi-stage process characterized by an unknown number of surges, with at least one smaller flow surge after the main one. Each surge might have been triggered by the exceedance of a load threshold exerted by stage 1 material pushed onto the steep slope, making a slowly moving stage 1 movement more likely.

We now consider the potential velocity of stage 2 of the SV Landslide:

i. Movement as an extremely rapid avalanching flow. The runout plane is very gently inclined towards SW, as shown by the contour lines in Fig. 2A. Any flow which is not moving extremely rapidly would be expected to turn toward the direction of steepest inclination when moving from the W-facing steep slope onto the SW-facing runout plane. Stage 2 of the SV Landslide, in contrast, maintained its flow direction. These findings support the hypothesis of an extremely rapid, quite suddenly stopping flow, with too much inertia to quickly change flow direction;
ii. Movement as a slow-rapid velocity flow. This hypothesis is supported by the fact that the lobate shape and steep frontal escarpments are consistent with a highly viscous, **"honey-like" type** of flow, such as slow-moving features on Earth, for example earth flows or rock glaciers (Fig. 8A). Some other similar structures on Earth, however, are related to processes of unknown velocity (Fig. 4B) or to presumably extremely rapid flow-type landslides (Fig. 4C). **Consequently, the available evidence does not allow a conclusive interpretation in terms of landslide velocity. The simulation results indicate the plausibility of an extremely rapid flow, but do not exclude the possibility of a slower movement.**

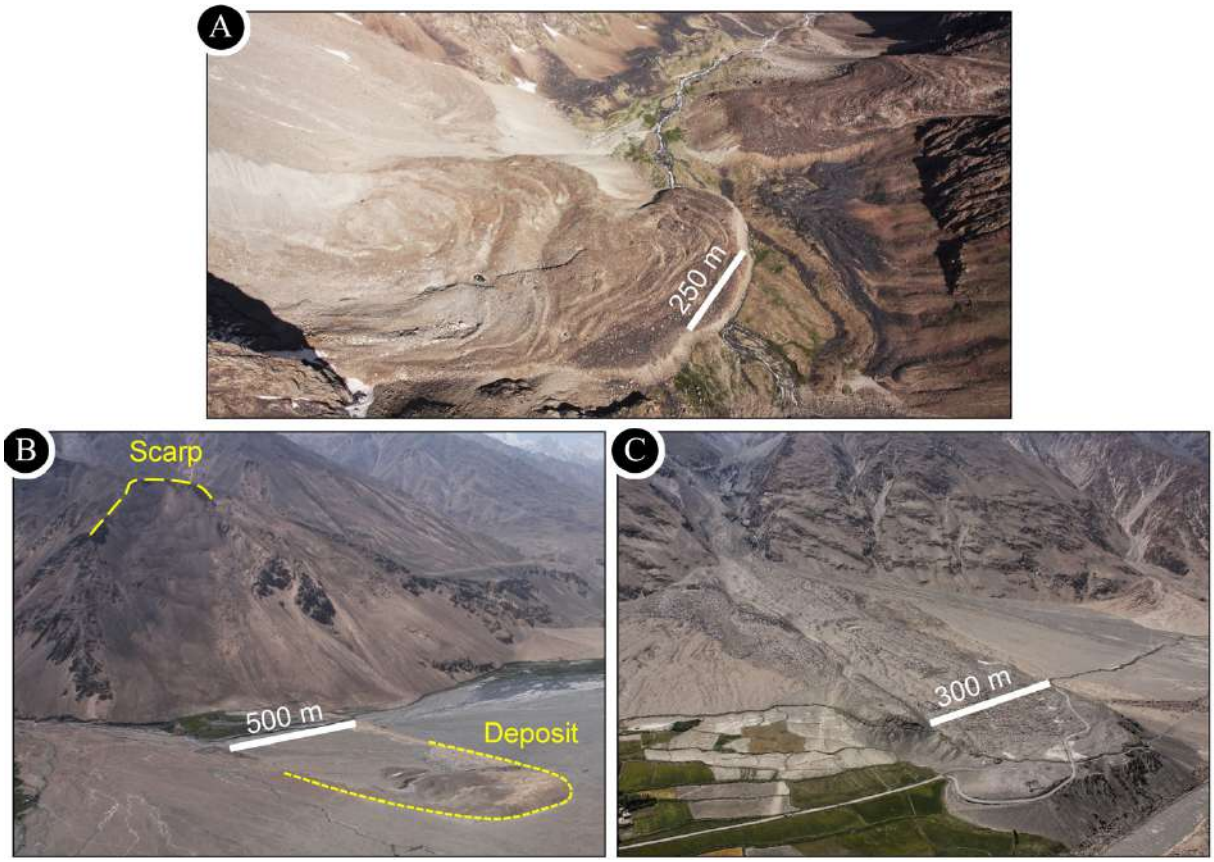

Fig. 8. Selected features of comparable size and pattern on Earth. A) Active rock glaciers in the Rushan Range (Pamir, Tajikistan). B) Ancient feature in the Vakhan Valley (Hindukush, Afghanistan), probably representing **the remnants of a landslide**. C) Tongue of a presumably extremely rapid debris avalanche near Ishkashim (Hindukush, Afghanistan). Photos: M. Mergili, 14 and 15 August 2009.

The best-fit *r.avaflow* simulation (Fig. 4), characterized by a high degree of empirical adequacy, presumes an extremely rapid stage 2 flow, which is suddenly released from the stage 1 deposit. All simulation attempts towards progressive release and/or a flow of lower velocity failed to reproduce the deposition patterns, as the simulated flows were clearly turning towards the direction of steepest slope in the deposition area – a behaviour even slightly visible in the best-fit result for an extremely rapid flow, clearly pointing towards the hypothesis II (Fig. 4A). **The values of the flow parameters (basal and internal friction, viscosity, yield strength) leading to the best correspondence of the *r.avaflow* simulation results with the observations (area, patterns of deposition height) are the outcome of an empirical optimisation procedure. We underline that these optimised parameter values should not be considered as physically correct material characteristics, as the optimisation outcome may be affected by possible equifinality issues, as well as by simplifications of the model assumptions. Hence, simulations on other Martian landslides with comparable characteristics will be necessary to draw conclusions on the general validity of that set of parameter values. Nevertheless, if we** compare our results with those obtained using a granular flow model presented by Guimpier et al. (2021), it is possible to notice that our simulated dynamical evolution returns a final deposit that is more similar to the observation in terms of the longitudinal profile, as well as for what concerns the formation of the lateral levees and the frontal shape. However, we note that *r.avaflow* is primarily designed for extremely rapid flows,

and, to our knowledge, there is also no other software available to properly simulate slow-rapidly moving flows, impeding a more rigorous numerical analysis of the corresponding scenarios.

As it is possible to see from Fig. 5, the identified boulders are not homogenously distributed along the landslide. As predicted by landslide particle size segregations (Crosta et al., 2007), where large particles generally move to the front and to the top surface, while the smaller particles accumulate at the bottom of the flow, the SV landslide's higher boulder spatial density is located at the forefront, where the biggest boulders with sizes larger than 20 m are also present. The lateral levees of the landslide are also two areas where the boulder density increases (Supplementary Material Fig. SM3), while the central part of the landslide is generally characterised by a depletion of boulders. Another location where the density of boulders increases is the rear side of the landslide, close to the reconstructed area where stage 2 might have started. It is likely that such boulders are the underneath remnant of the landslide mass that detached during stage 1.

From the boulder SFD analysis we find that the power-law curve adequately fits the SFD at the smallest sizes in the range 1.75 - 3.2 m, with a power-law index of -1.77, nevertheless it underestimates the values from 3 to 10 m, as well as severely overestimates the data > 10 m (Fig. 7). In contrast, the exponential-law fit underestimates values between < 3 m and > 10 m, while overestimating the sizes that are found in the middle. For this reason, this curve can hardly be considered as a good fitting one for the observed data. The Weibull curve, instead, show a very good fit to the data in the whole size range considered (Fig. 7).

From a formative perspective, the power-law SFD would indicate a single-event fragmentation (for example during impact cratering) that leads to a branching tree of cracks that have a fractal character (Turcotte et al., 1997, Schröder et al., 2021b). Whereas, the Weibull distribution is thought to result from sequential fragmentation (Brown & Wohletz 1995) and it is largely used in fracture and fragmentation theory (Grady and Kipp, 1987; Brown and Wohletz, 1995; Turcotte, 1997; McSaveney, 2002). In addition, the Weibull distribution (Weibull, 1951) is often used to describe the particle distribution that is derived from grinding experiments (Rosin and Rammler, 1933). The good fit between the boulder SFD and the Weibull curve may therefore suggest that while the SV landslide formed and was moving downward as a single event, the rocky constituents may have been ground in a sequential way (McSaveney, 2002), rather than in a sudden, single-event fragmentation (as, for example, boulders that are formed during impacts), hence resulting in the distribution that we see today.

Some of the largest identified boulders show exposed deep cracks and fractures dividing them into separate chunks (Supplementary Material Fig. SM2 A-D). As shown by Eppes et al. (2015), simple diurnal insolation can drive subcritical fracture growth in Martian rocks, that can afterwards result in polygonal pattern of cracking and hence a disintegration of the boulder into pieces. Moreover, de Hass et al. (2013) estimated that the boulder local breakdown rate due to the presence of (metastable) liquid water during the last glacial period of Mars is of 3.5 m/Ma. So, despite the young age of the SV landslide (~ 4.5 $\pm$ 4 Ma, Guimpier et al., 2021) favouring the preservation of the original boulders SFD, it could be affected by secondary weathering processes.

We do not think that solar-induced thermal stress can explain all the observed fractures because we do not observe the mentioned developed polygonal cracking in the boulders (at least at the 0.25 m spatial scale) and the cracks we identify are randomly oriented, which should not be the case for solar-induced cracks. Moreover, the boulders in the SV deposit look particularly fresh with sharp shapes, and only a small proportion (a few tens) of the total number is affected by fractures, hence pointing to recent boulder formation

from the parent bedrock. Concerning the local boulder breakdown rate, de Haas et al. (2013) mentioned that this value is site specific and it was identified on a small alluvial fan system in eastern Promethei Terra, which is a different morphological setting to the one studied here. In addition, it is not clear if metastable liquid water enhancing weathering rates was ever present on the SV landslide deposit given its equatorward latitude.
For all such mentioned reasons, we maintain that the derived SFD reflects the original one, nevertheless, we cannot rule out that an in-situ form of weathering is actually occurring in the SV deposit, at least on the biggest boulders.

We highlight that both the simulation reported in this paper, as well as the boulder SFD study do not analyse the triggering causes of the landslide, which is a difficult matter to identify and unambiguously prove (Crosta et al., 2014; Kumar et al., 2019; Bishop et al., 2021). Indeed, as presented by Guimpier et al. (2021), both seismic shaking from a nearby meteorite impact, or from a crustal marsquake could have been triggers for this landslide, but other processes such as those related to thermal stress cannot be ruled out, either (Tesson et al., 2020). However, one could hypothesize as predisposing factor the presence of a structural weakness in the landslide area, as evidenced by the local irregularity of the mesa edge. Indeed, Guimpier et al. (2021) suggested that the raised topography near to the landslide scarp could be the remnants of a rim of an ancient impact crater that formed before the incision of the Simud Vallis outflow channel. If this is the case, it could point out at a location of pre-existing weakness. Moreover, the occurrence of localised darker-than-the-surroundings colour in close proximity to the circular eroded area could hint at a different mineralogical composition, too. Whether this suggests the presence of hydrated materials or not is a matter of debate, since this area is affected by the presence of dust and no unambiguous hydrated mineral signatures have been identified here (Pajola et al., 2016a). But if so, this could support the hypothesis of a reduced local strength. Eventually, structural weakness in the mesa could also be hypothesized due to the deep excavated trenches visible at the back of the landslide scarp (Fig. 1C).

Conclusions

We have studied a young (~ 4.5 $\pm$ 4 Ma), 3.4 km long landslide located on the floor of Simud Vallis on Mars that was previously analysed by Guimpier et al. (2021). This previous work **included** a *SHALTOP* numerical modelling of the landslide movement, but acknowledged that the results obtained were not conclusive since the simulated deposits differed from the **observed** landform appearance.

Based on the visual criteria, the Simud Vallis landslide can be interpreted as a complex landslide involving both a rotational slide (stage 1) and a flow (stage 2). Using a **2 m-scale** HiRISE DEM we have reconstructed the initial terrain surface, allowing us to estimate the release and deposition heights and volumes related to the different stages of the landslide. For stage 1, we suggest a rotational slide with a total volume of $54.0 \cdot 10^6$ m^3. Most of this initial volume was then involved in the stage 2 flow, whereas $13.4 \cdot 10^6$ m^3 of it remained perched in the source area. The post-event DEM revealed a stage 2 deposition volume of $48.7 \cdot 10^6$ m^3, indicating a volume increase of 20% with respect to the stage 2 release value, due to the generation of pore space during the flow. This confirms the overall plausibility of the reconstruction, even though the exact shape of the stage 1 deposition and the stage 2 release mass remain uncertain.

The stage 2 flow has been numerically reconstructed with the *r.avaflow* software. The general patterns of the flow, including the formation of a steep frontal scarp and lateral levees, is reproduced by the simulation. Nevertheless, we highlight that the height of the modelled deposit is slightly overestimated in the frontal part, since our model result does not include the assumed 20% pore space of the observed deposit. Moreover, when compared to the **observed** deposit, our simulation results show a very slight southward turn of the mass in the relatively flat deposition area. Our best-fit simulation suggests an extremely rapid stage 2 flow, which is suddenly released from the stage 1 deposit. This is supported by the fact that the landslide deposit exhibits a set of trenches that align parallel to the local direction of motion, indicative of a likely rapid-to fast-moving flow mechanism for the emplacement of failed materials. **The simulated impact area based on *r.avaflow* clearly shows a higher degree of correspondence to the observed impact area of the Simud Vallis landslide than the simulated impact area based on *SHALTOP* (Guimpier et al., 2021). We attribute this improved model performance to a more appropriate definition of the release mass, as well as to the assumption of a viscous flow, which is most probably more realistic than the assumption of a purely frictional flow, as it was applied by Guimpier et al. (2021) based on the scope of the SHALTOP software.**

By using two 0.25 m-scale HiRISE images we have manually identified and counted > 130 000 boulders located along the landslide. As predicted by landslide particle size segregations, the identified boulders are not homogenously distributed along the landslide. The highest spatial density of boulders is located at the front of the deposit, where the biggest boulders with sizes larger than 20 m are also present. The boulder density increases also inside the lateral levees of the landslide as well as where the remnants of the mass that detached during stage 1 is present. After deriving the boulder size-frequency distribution in the size range 1.75-59.2 m (the total number of boulders ≥ 1.75 m being 24 073), we have identified that the best fitting curve is the Weibull distribution which results from sequential fragmentation and it is often used to describe the particle distribution derived from grinding experiments. This suggests that while the Simud Vallis landslide formed and was moving downslope, it could have ground the rocky constituents in a sequential way, rather than in a sudden, single-event fragmentation.
The analyses done in this paper did not aim to identify the triggering causes of the landslide. Nevertheless, we could hypothesize as the landslide predisposing factor the presence of structural weaknesses in the collapsed area, as i) the irregularity of the mesa edge that can hint at an ancient impact crater that formed before the incision of the Simud Vallis outflow channel, ii) the occurrence of the deep excavated trenches visible at the back of the landslide scarp, as well as iii) the possible presence of a different local mineralogy, all favouring a reduced local strength.

Eventually, we underline that the characterisation of the boulder SFD, coupled with the modelling of the landslide movement is a novel approach that can be used for future analyses of mass movements and boulder fragmentation that occurred in the Late Amazonian period of Mars.

Acknowledgements

The authors are grateful to Dr. Rishitosh K. Sinha and to an anonymous Reviewer for constructive and important comments, suggestions and corrections, that lead to a substantial improvement of the paper. This study has been supported by the Italian Space Agency (ASI-INAF agreement no. 2020-17-HH.0). We would like to thank Dr. Lorenzo Marchi

for helpful discussions on terrestrial analogues, and Dr. Emanuele Baratti for useful discussions on fitting curve techniques. AG is grateful for the support of the Programme National de Planétologie.

References

Bart, G.D.; Melosh, H. 2010. Distributions of boulders ejected from lunar craters. Icarus, 209, 337–357.

Beddingfield, C.B. et al., 2021. Landslides on Charon. Icarus, 335, 113383.

Bigot-Cormier, F. and Montgomery, D. R., 2007. Valles Marineris landslides: evidence for a strength limit to Martian relief? Earth Planet. Sci. Lett. 260, 179–186. https://doi.org/j.epsl.2007.05.028.

Bishop, J. L. et al., 2021. Martian subsurface cryosalt expansion and collapse as trigger for landslides. Science Advances 7(6), eabe4459. https://doi.org/10.1126/sciadv.abe4459.

Blewett, D. T. et al., 2013. Mercury's hollows: Constraints on formation and composition from analysis of geological setting and spectral reflectance. J. Geophys. Res. Planets 118, 1013–1032.

Bouchut, F., et al., 2003. A new model of Saint Venant and Savage–Hutter type for gravity driven shallow water flows. Comptes Rendus Math. 336, 531–536.

Bouchut, F. and Westdickenberg, M., 2004. Gravity driven shallow water models for arbitrary topography. Commun. Math. Sci. 2, 359–389.

Brown, W.K. and Wohletz, K.H., 1995. Derivation of the Weibull distribution based on physical principles and its connection to the Rosin-Rammler and lognormal distributions. J. Appl. Phys. 78, 2758–2763.

Brunetti, M. T., et al., 2014. Analysis of a new geomorphological inventory of landslides in Valles Marineris, Mars. Earth Planet. Sci. Lett. 405, 156–168.

Brunetti, M. T. et al., 2015. Large rockslides in impact craters on the Moon and Mercury. Icarus, 260, 289–300.

Burrough P.A. and McDonnell R.A., 1998. Principles of Geographical Information Systems. Oxford University Press, New York.

Burke, K.N. et al., 2021. Particle Size-Frequency Distributions of the OSIRIS-REx Candidate Sample Sites on Asteroid (101955) Bennu. Remote Sens., 13, 1315.

Carr, M.H. and Clow, G.D., 1981. Martian channels and valleys: Their characteristics, distributions, and age. Icarus, 48 (1), 91–117.

Chuang, F.C. and Greeley, R., 2000. Large mass movements on Callisto. J. of Geophys. Res. 105(E8), 20227-20244.

606 Cintala, M.J.; McBride, K.M. 1995. Block Distributions on the Lunar Surface: A Comparison
607 between Measurements Obtained from Surface and Orbital Photography. In NASA Technical
608 Memorandum 104804. Available online: https://www.lpi.usra.edu/
609 lunar/documents/NASA_TM_104804_Lunar_blocks.pdf

610 Crosta, G. B., et al., 2007. Fragmentation in the Val Pola rock avalanche, Italian Alps. Journal
611 of Geophysical Research, 112, F01006.

612 Crosta, G. B., et al., 2014. Reassessing rock mass properties and slope instability triggering
613 conditions in Valles Marineris, Mars. Earth Planet. Sci. Lett. 388, 329–342.

614 Crosta, G. B. et al., 2018. Introducing a new inventory of large Martian landslides. Earth and
615 Space Science, 5(4), 89–119. https://doi.org/10.1002/2017EA000324.

616 Cruden, D. M. and Varnes, D. J. (1996). Landslide types and processes. In: Turner, A.K.,
617 Schuster, R.L. (Eds.), Landslides, Investigation and Mitigation. In: Transportation Research
618 Board Special Report 247. Washington D.C., pp.36–75.

619 **de Haas, T., Hauber, E. and Kleinhans, M.G., 2013. Local late Amazonian boulder**
620 **breakdown and denudation rate on Mars. Geophysical Research Letters, 40(14), pp.3527-**
621 **3531.**
622
623 Duarte, K. D., et al., 2019. Landslides on Ceres: Diversity and geologic context. Journal of
624 Geophysical Research: Planets, 124, 3329-3343.
625
626 Eppes, M-C. et al., 2015. Cracks in Martian boulders exhibit preferred orientations that point
627 to solar-induced thermal stress. Nature Communications, 6:6712, 1-11.

628 Garvin, J.B. et al., 1981. Characterization of rock populations on planetary surfaces: Techniques
629 and a preliminary analysis of Mars and Venus. Earth Moon Planets, 24, 355–387.
630
631 Geissler, P.; et al., 1996. Erosion and Ejecta Reaccretion on 243 Ida and Its Moon. Icarus, 120,
632 140–157.
633
634 Golombek, M. and Rapp, D., 1997. Size-frequency distributions of rocks on Mars and Earth
635 analog sites: implications for future landed missions. J. Geophys. Res. 102, 4117–4129.
636
637 Golombek, M.P. et al., 2008. Size-frequency distributions of rocks on the northern plains of
638 Mars with special reference to Phoenix landing surfaces. J. Geophys. Res. Space Phys., 113.
639
640 Grady, D.E. and Kipp, M.E., 1987. Dynamic rock fragmentation. In: Atkinson, B.K. (Ed.),
641 Fracture Mechanics of Rock. Academic Press, London, U.K, pp. 429–475.
642
643 Grant, J.A., et al., 2006. Distribution of rocks on the Gusev Plains and on Husband Hill, Mars.
644 Geophys. Res. Lett., 33, 16202.
645
646 Guimpier, A., et al., 2021. Dynamics of recent landslides (<20 My) on Mars: Insights from
647 high-resolution topography on Earth and Mars and numerical modelling. Planetary and Space
648 Science, 206, 105303.

649 Guzzetti, F., et al., 2012. Landslide inventory maps: new tools for an old problem. Earth-Sci.
650 Rev.112 (1–2), 42–66.

Hargitai, H., and Kereszturi, A, 2015. Encyclopedia of Planetary Landforms, by H. Hargitai and A. Kereszturi. ISBN 978-1-4614-3133-6. Berlin: Springer-Verlag, 2015.

Hungr, O., et al., 2014. The Varnes classification of landslide types, an update. Landslides, 11(2), 167–194.

Jawin, E. R. et al., 2020. Global patterns of recent mass movement on asteroid (101955) Bennu. Journal of Geophysical Research: Planets, 125, e2020JE006475.

Krishna, N. and Kumar, P.S. 2016. Impact spallation processes on the Moon: A case study from the size and shape analysis of ejecta boulders and secondary craters of Censorinus crater. Icarus, 264, 274–299.

Kumar, P.S., et al., 2019. Recent seismicity in Valles Marineris, Mars: Insights from young faults, landslides, boulder falls and possible mud volcanoes. Earth Planet. Sci. Lett. 505, 51–64.

Küppers, M.; et al., 2012. Boulders on Lutetia. Planet. Space Sci., 66, 71–78.

Lindsay, J., 1976. Energy at the lunar surfaces. In: Kopal, Z., Cameron, A.G.W. (Eds.), Lunar Stratigraphy and Sedimentology. Developments in Solar System and Space Science, vol. 3. Elsevier, pp. 45–55.

Lucas, A. and Mangeney, A., 2007. Mobility and topographic effects for large Valles Marineris landslides on Mars. Geophys. Res. Lett. 34, L10201.

Lucchetti, A. et al., 2019. The rocky-like behavior of cometary landslides on 67P/Churyumov-Gerasimenko. Geophys. Res. Lett. 46, 14336-14346.

Lucchitta, B. K., 1979. Landslides in Valles Marineris, Mars. J. Geophys. Res.84 (B14), 8097–8113.

Magrin, S. et al., 2012. (21) Lutetia spectrophotometry from Rosetta-OSIRIS images and comparison to ground-based observations. Planetary and Space Science, 66, 43-53.

Malin, M. C., 1992. Mass movements on Venus: Preliminary results from Magellan cycle 1 observations. J. Geophys. Res. Planets 97, 16337–16352.

Massironi, M. et al., 2012. Geological map and stratigraphy of asteroid 21 Lutetia. Planetary and Space Science, 66, 125-136.

Mastropietro, M.; et al., 2020. Boulder Analysis on the Oxia Planum ExoMars 2022 Rover Landing Site: Scientific and Engineering Perspectives. Sol. Syst. Res., 54, 504–519.

Mazrouei, S. et al., 2014. Block distributions on Itokawa. Icarus 2014, 229, 181–189.

Michael, G.G., Neukum, G., 2010. Planetary surface dating from crater size frequency distribution measurements: Partial resurfacing events and statistical age uncertainty. Earth Planet. Sci. Lett. 294, 223–229.

Moratto, Z.M., et al., 2010. Ames stereo pipeline, NASAs open source automated stereogrammetry software. In: Proceedings of the 41st Lunar and Planetary Institute Science Conference. Houston, Texas [2364].

694 Mottola, S. et al., 2015. The structure of the regolith on 67P/Churyumov-Gerasimenko from
695 ROLIS descent imaging. Science 2015, 349, aab0232.

696 McEwen, A. S., 1989. Mobility of large rock avalanches: evidence from Valles Marineris,
697 Mars. Geology 17, 1111–1114.

698 McEwen, A.S. et al., 2007. Mars Reconnaissance Orbiter's high resolution imaging science
699 experiment (HiRISE). J. Geophys. Res. 112, E05S02.
700
701 McSaveney, M. J., 2002. Recent rockfalls and rock avalanches in Mount Cook National Park,
702 New Zealand, in Catastrophic Landslides: Effects, Occurrence, and Mechanisms: Reviews in
703 Engineering Geology, edited by S. G. Evans and J. V. DeGraff, Geol. Soc. Am. Rev. Eng.
704 Geol., XV, 35– 70.
705
706 Mergili, M., et al., 2017. r.avaflow v1, an advanced open source computational framework for
707 the propagation and interaction of two-phase mass flows. Geoscientific Model Development
708 10: 553-569. doi:10.5194/gmd-10-553-2017

709 Mergili, M. and Pudasaini, S.P., 2021. r.avaflow – The mass flow simulation tool.
710 https://www.avaflow.org. Last access: 5 March 2021.

711 Michikami, T. et al., 2008. Size-frequency statistics of boulders on global surface of asteroid
712 25143 Itokawa. Earth Planets Space 60, 13–20.
713
714 Neukum, G., Jaumann, R., 2004. HRSC: the High Resolution Stereo Camera of Mars Express
715 1240, 17–35.
716
717 Pajola, M. et al., 2015. Size-frequency distribution of boulders >=7 m on comet
718 67P/Churyumov-Gerasimenko. Astron. Astrophys. 2015, 583, A37.
719
720 Pajola, M. et al., 2016a. The Simud–Tiu Valles hydrologic system: A multidisciplinary study
721 of a possible site for future Mars on-site exploration. Icarus 268, 355-381.
722
723 Pajola, M.; et al., 2016b. Size-frequency distribution of boulders >= 10 m on comet
724 103P/Hartley 2. Astron. Astrophys. 2016a, 585, A85.
725
726 Pajola, M., et al., 2016c. The southern hemisphere of 67P/Churyumov-Gerasimenko: Analysis
727 of the pre-perihelion size-frequency distribution of boulders >=7 m. Astron. Astrophys. 2016b,
728 592, 2.
729
730 Pajola, M. et al., 2017a. The pristine interior of comet 67P revealed by the combined Aswan
731 outburst and cliff collapse. Nat. Astron. 2017, 1, 0092.
732
733 Pajola et al., 2017b. The pebbles/boulders size distributions on Sais: Rosetta's final landing site
734 on comet 67P/Churyumov-Gerasimenko. MNRAS 469, S636-S645.
735
736 Pajola et al., 2017c. Boulder abundances and size-frequency distributions on Oxia Planum-
737 Mars: Scientific implications for the 2020 ESA ExoMars rover. Icarus, 296, 73–90.
738
739 Pajola, M.; et al., 2019. Abundance and size-frequency distribution of boulders in Linné crater's
740 ejecta (Moon). Planet. Space Sci. 2019, 165, 99–109.
741

Pajola et al., 2021. Blocks Size Frequency Distribution in the Enceladus Tiger Stripes Area: Implications on Their Formative Processes. Universe 2021, 7, 82.

Peruzzetto, M. et al., 2021. Simplified simulation of rock avalanches and subsequent debris flows with a single thin-layer model. Application to the Prêcheur river (Martinique, Lesser Antilles), EGU General Assembly 2021, online, 19–30 Apr 2021, EGU21-2752, https://doi.org/10.5194/egusphere-egu21-2752, 2021.

Pierson, T. C. and Costa, J. E., 1987. A rheologic classification of subaerial sediment-water flows. Geological Society of America Reviews in Engineering Geology7, 1–12.

Pike, R. J., 1971. Some preliminary interpretations of lunar mass-wasting process from Apollo 10 photography. In: Analysis of Apollo 10 Photography and Visual Observations. NASA SP-232, Washington, DC, pp. 14–20.

Pudasaini, S.P. and Mergili, M., 2019. A Multi-Phase Mass Flow Model. JGR Earth Surface 124(12): 2920-2942. doi:10.1029/2019JF005204

Rosin, P., & Rammler, E. 1933. The laws governing the fineness of powdered coal. Journal of the Institute of Fuel, 7, 29.

Quantin, C., et al., 2004. Morphology and geometry of Valles Marineris landslides. Planet. Space Sci. 52 (11), 1011–1022.

Schenk, P. M. and Bulmer, M. K., 1998. Origin of mountains on Io by thrust faulting and large-scale mass movements. Science 279, 1514–1517.

Schröder, S.E. et al., 2021a. The Boulder Population of Asteroid 4 Vesta: Size-Frequency Distribution and Survival Time. Earth Space Sci. 2021, 8, 000941.

Schröder, S.E. et al., 2021b. The Brittle Boulders of Dwarf Planet Ceres. The Planetary Science Journal, 2: 111, 15 pp.

Shaller, P. J. and Komatsu, G., 1994. Landslides on Mars. Landslide News 8, 18–22.

Sharp, R.P., 1973. Mars: Troughed terrain. J. Geophys. Res. 1896-1977 78, 4063–4072.

Shi, X., J. et al., 2016. Mass wasting on Phobos triggered by an evolving tidal environment, Geophys. Res. Lett., 43, 12,371–12,379, doi:10.1002/2016GL071650.

Singer, K. N. et al., 2012. Massive ice avalanches on Iapetus mobilized by friction reduction during flash heating. Nature Geoscience. 5, 574-578.

Soukhovitskaya, V. and Manga, M. (2006). Martian landslides in Valles Marineris: wet or dry? Icarus, 180, 348–352.

Tanaka, K.L. et al., 2014. Geologic Map of Mars, Reston, Va.: US Geological Survey, 2014.

Tesson, P. A., et al., 2020. Evidence for thermal-stress-induced rockfalls on Mars impact crater slopes. Icarus 342, 113503.

Thomas, P.C. et al., 2001. Shoemaker crater as the source of most ejecta blocks on the asteroid 433 Eros. Nat. Cell Biol., 413, 394–396.

Turcotte, D.L., 1997. Fractals and Chaos in Geology and Geophysics, second ed. Cambridge University Press, Cambridge.

Xiao, Z., et al., 2013. Mass wasting features on the Moon—How active is the lunar surface? Earth Planet. Sci. Lett. 376, 1–11.

Xiao, Z. and Komatsu, G. 2013. Impact craters with ejecta flows and central pits on Mercury, Planetary and Space Science, vol. 82-83, pp. 62-78.

Weibull, W., 1951. A statistical distribution function of wide applicability, J. Appl. Mech., 18, 837– 843.

Wingo, D. R. 1989. The left-truncated Weibull distribution: theory and computation. Statistical Papers, 30, 39.

Zurek, R.W. et al., 2007. An overview of the Mars Reconnaissance Orbiter (MRO) science mission. J. Geophys. Res. 112 (E5), CiteID E05S01.

Supplementary Material

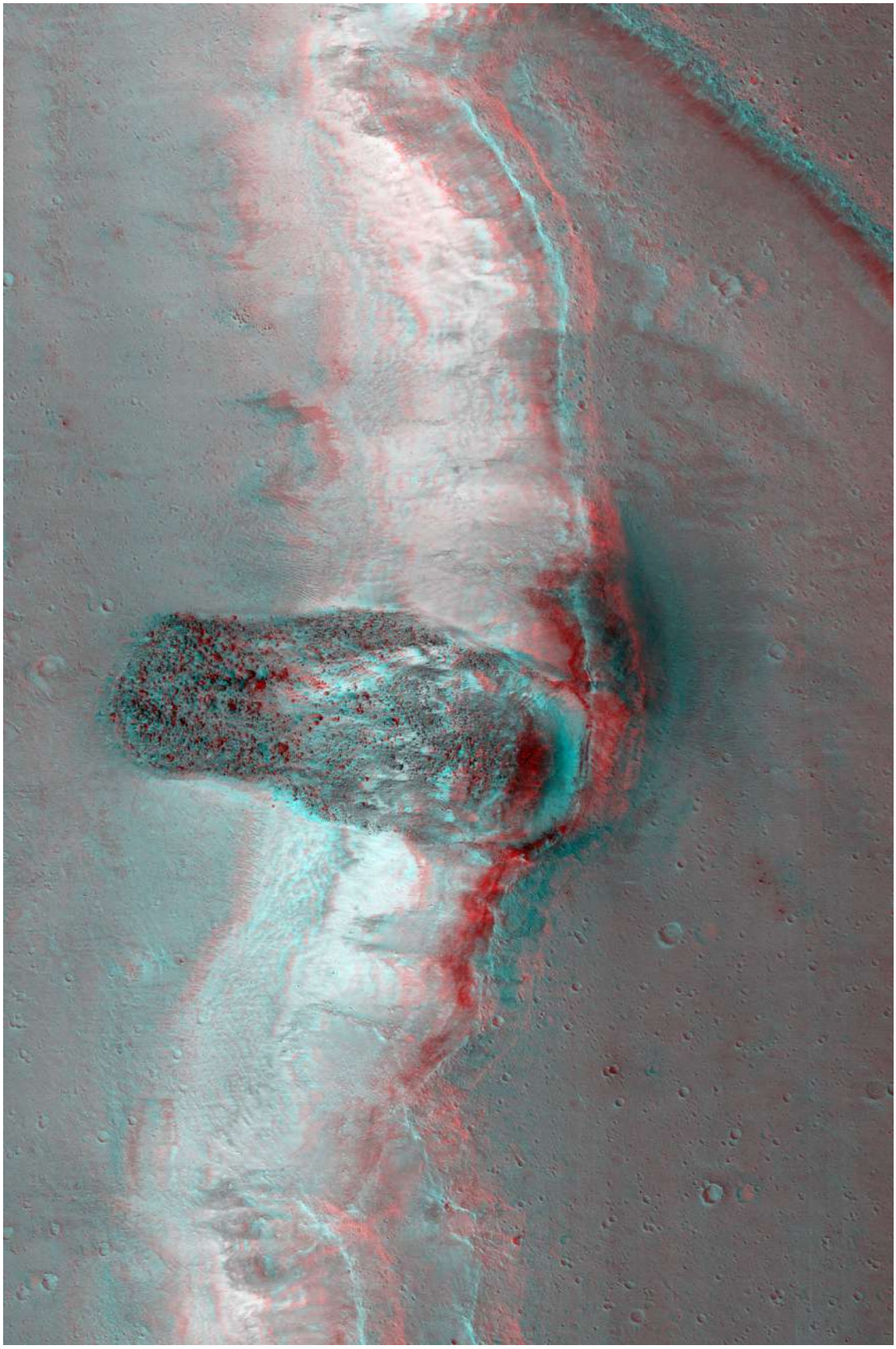

Figure SM1: The anaglyph obtained with the two HiRISE images presented in Table 1.

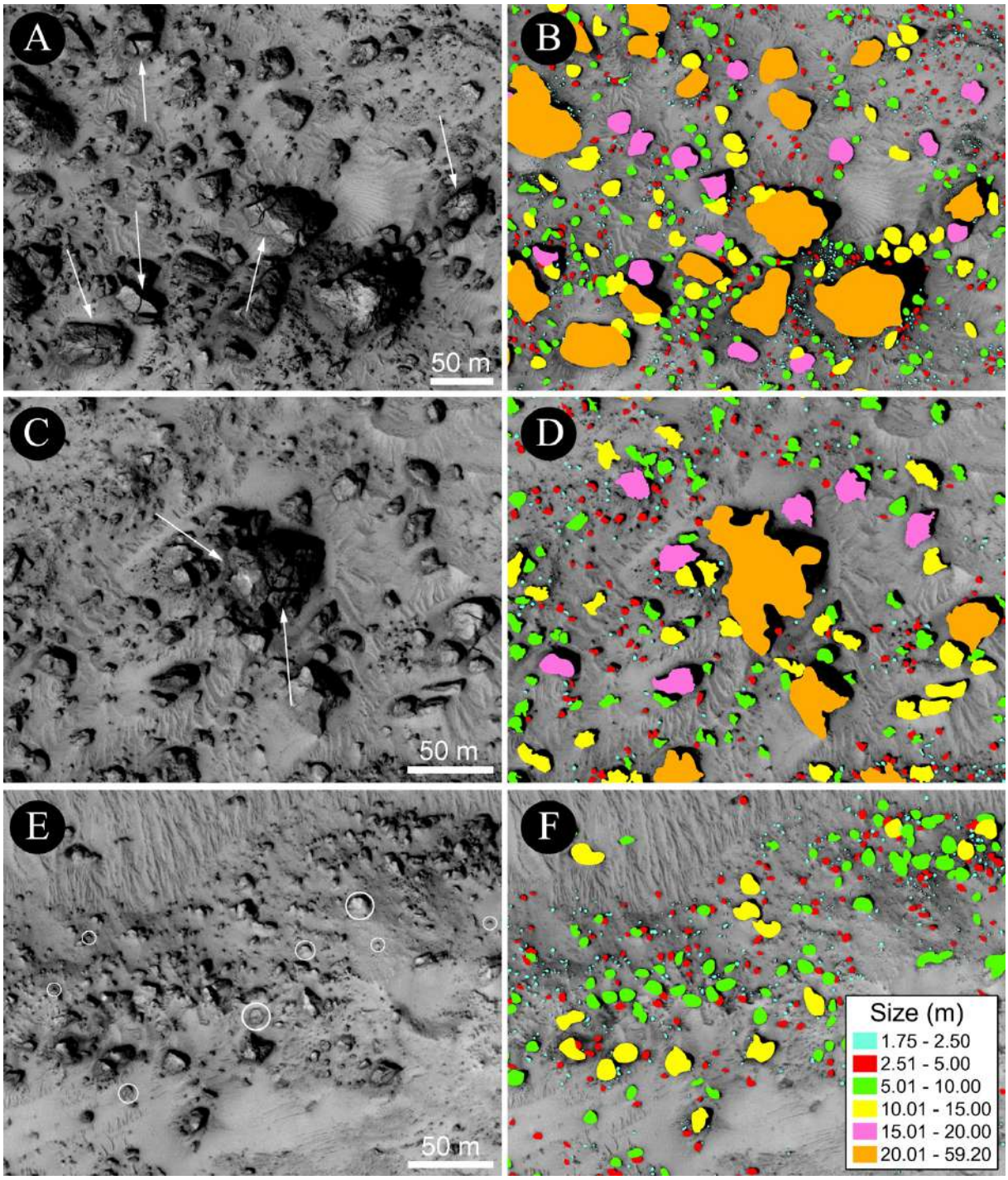

Figure SM2: A-D) Close-up figures showing the fractured boulders (indicated with white arrows) mentioned in the main text. As it is possible to see all chunks belonging to the same fractured boulder are identified as a single boulder. E-F) The boulders (identified with white circles) that are partially covered by dust.

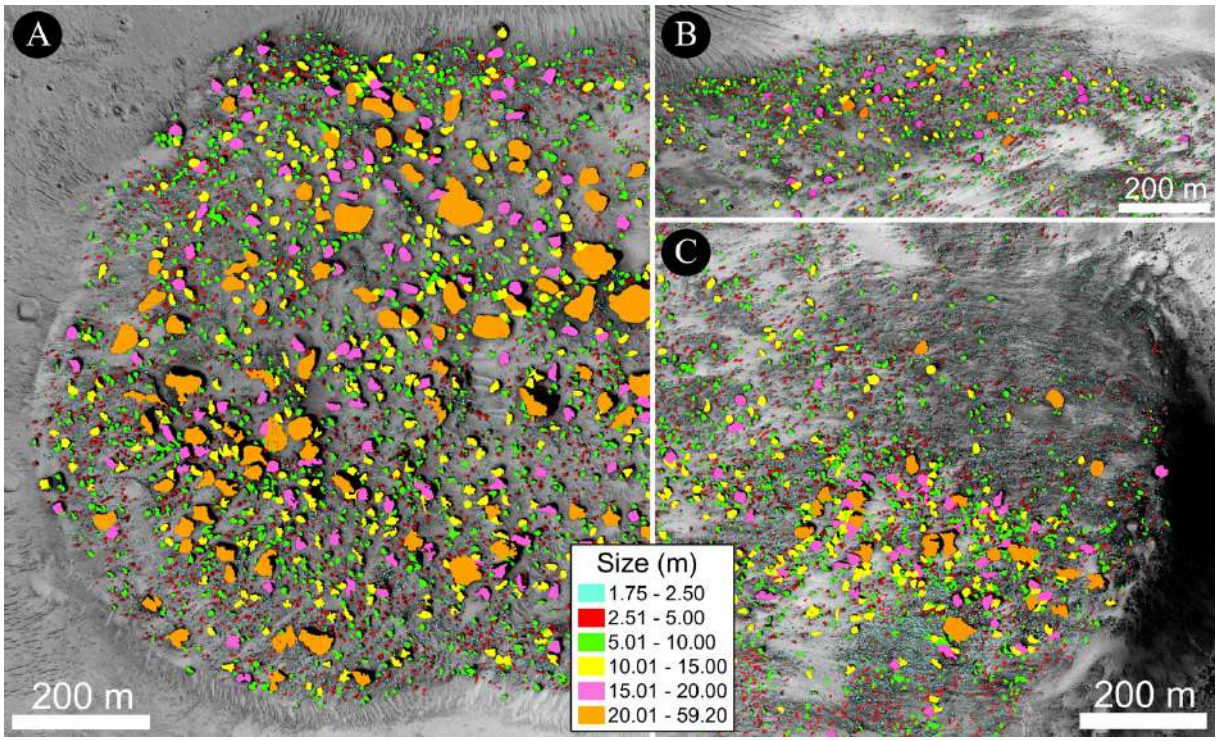

Figure SM3: Close-up figures showing the boulders ≥ 1.75 m presented in Fig. 5. A) Frontal part of the SV landslide. B) Upper lateral levee of the landslide. C) Rear side of the SV landslide.